Lens Opacities Classification System III-Based Computational Model of Nuclear Cataracts

Chi-Hung Lee and George C. Woo

***Abstract*—This study developed a computational model to assess the optical properties of nuclear cataracts, using slit-lamp lens images for clinical evaluation based on color and opacity. Cataracts were represented as spherical particles distinct from the surrounding lens medium, with diameters ranging from tens to hundreds of nanometers. This study examined the effects of particle diameter, concentration, and colorimetric properties on the opacity of cataracts and their relationship with images on the retina. The findings indicate that particle size and concentration influence opacity. To ensure alignment with the Lens Opacities Classification System III, colors were defined based on a color absorption coefficient limited within a predetermined range. The developed model was used to simulate the yellow-tinted vision experienced by patients with nuclear cataracts.**

***Index Terms*—Model, cataract, slit-lamp, opacity, color.**

I. Introduction

CATARACTS are dense protein particles that cloud the lens of the eye and result in blurred retinal images. They can be induced by aging, smoking, ultraviolet radiation, long-term steroid use, specific medications, diabetes, and trauma. If left untreated, they greatly increase the risk of blindness. Clinically, cataracts are classified as nuclear, subcapsular, or cortical based on their opacity [1]. The most prevalent type of cataract is nuclear cataracts, which are distinguished by the aggregation of proteins within the eye's nucleus. The size and concentration of particles within these aggregations determines the extent of light scattering, resulting in distinct optical effects. Larger particles within the aggregation can act as deflection agents, redirecting forward light and contributing to phenomena like retinal straylight [2], [3], [4], [5], [6]. On the other hand, smaller particles exhibit a propensity to scatter light in a multitude of random directions, which can be used to judge the severity of cataract. Nuclear cataracts are diagnosed and graded through the comparison of slit-lamp images with a set of standard photographs with increasing opacity and lens nucleus color [7]. Such images are formed by light scattered backward by the smaller particles [8], [9], [10]. Researchers studying cataracts and related eye conditions can benefit from knowing particle sizes and concentrations. This information can contribute to a deeper understanding of the underlying causes and mechanisms of cataract formation, potentially leading to the development of more effective treatments and interventions in the field of ophthalmology. However, there is a difficulty to estimate the particle size because large and small particles coexist within the same areas of the crystalline lens, and their proportions may vary. To estimate the size and concentration of particles, researchers directly analyze lens tissue samples, but this method is invasive and not practical for clinical use [3].

Based on measurement data from previous literatures, photometry and color science, this study developed a computational approach to quantify the concentration and absorption spectra of particles within each color and opalescence category of the Lens Opacities Classification System III (LOCS III). For simplification, our approach initially evaluated the concentration of large particles and then that of the small particles at first. After obtaining the possible concentration values of the particles, we proceeded to consider the interaction between the two particle sizes. The structure of Section II is as the following: Section II-A focuses on the relationship between the concentration of large scattering particles and contrast acuity scores, a characteristic tied to forward scattering. Section II-B describes the analysis of the luminance and color of six slit-lamp images for grading nuclear color (NC) and nuclear opalescence (NO) in accordance with LOCS III. Section II-C discusses the distribution of backward-scattered light and the resulting effect of the density of small particles within the lens. This section also discusses a series of images simulated to illustrate the backward-scattered light distribution as captured by a microscope. Finally, Section II-D presents the traits of both backward and forward scattering simulated for each LOCS III grade, considering both small and large scattering particles as well as the absorption spectra of lens pigments.

II. Computational Model

A. Modeling Forward Scattering by Large Particles

Kelly constructed a computational model for simulating forward scattering from particles within a cataract inside the lens nucleus [11]. In this model, the scattering particles are spherical bodies possessing a refractive index distinct from that of the lens medium enveloping them. Following van den Berg [3], we used optical software, LightTools [12], to construct the biometry in a Walker schematic eye model [13] and examine the correlation between forward scattered light, which influences retinal images

Manuscript received 8 August 2023; revised 4 September 2023; accepted 22 September 2023. Date of publication 26 September 2023; date of current version 19 October 2023. *(Corresponding author: Chi-Hung Lee.)*

Chi-Hung Lee is with the Department of Electrical Engineering, Feng-Chia University, Taichung 40724, Taiwan (e-mail: chihlee@fcu.edu.tw).

George C. Woo is with the School of Optometry, Center for Eye and Vision Research, The Hong Kong Polytechnic University, Hong Kong SAR, China (e-mail: george.woo@polyu.edu.hk).

Digital Object Identifier 10.1109/JPHOT.2023.3319393

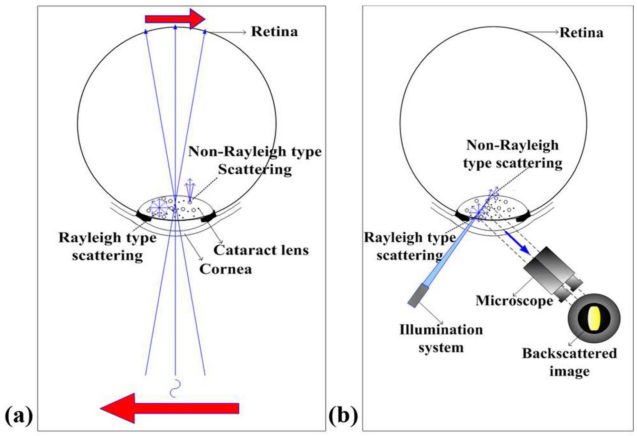

Fig. 1. Schematic eye model with scattering particles inside the crystalline lens. (a) The large type induces non-rayleigh scattering, primarily occurring in the forward direction, which is crucial for vision. (b) The small type induces rayleigh scattering, resulting in the scattering of light in various directions. When using an illumination system to shine light on the lens, backward-scattered light can be captured by a microscope. These images can be used to judge the severity of cataract.

(Fig. 1(a)), and backward-scattered light as a measure of cataract severity (Fig. 1(b)).

In the model eye, spherical protein particles were evenly distributed throughout the lens. There are two primary types of scattering particles (as defined by van den Berg [3]) present in the lens: a small type with a 10-nm radius and a large type with a radius of approximately 0.7 μm. We set the refractive indices of the lens material and cataract particles to 1.411 and 1.5017, respectively. Using data from van den Berg [14], we determined that the large-particle concentrations in the densest region are 19000 mm^{-3} for a nuclear cataractous lens of NO of 1.6 (NC of 2.8) and 525000 mm^{-3} for a lens of NO of 5.0 (NC of 6.2). These values imply that the range of the large-particle concentration of a lens with nuclear cataracts is 0–1000000 mm^{-3}. To assess the relationship between large-particle concentration and NO, we referred to Stifter's study [15], in which early, intermediate, and advanced nuclear cataracts were associated with significantly reduced contrast acuity scores. The average contrast acuity scores (LogMAR) for a 100% contrast level should be −0.07, 0.08, 0.22, 0.38, 0.52, and 0.67 for LOCS III grades NO1 to NO6, respectively. Hecht demonstrated that visual acuity generally varies in accordance with the logarithm of illumination (Log I) [16]. This relationship, however, is not strictly linear but follows a sigmoid pattern, indicating the existence of saturation points for human visual acuity under extreme lighting conditions. To translate this concept into a practical tool for our study, we converted LogMAR values into visual acuity, which we further translated into illumination measurements in millilamberts and nits. These conversions are presented in Table I. The penultimate column, "Relative T. R.," lists the ratios of the transmittance of eyes with various NO types to that of a healthy eye.

We executed optical simulations testing a series of large-particle concentrations inside the lens of the model eye. The simulations revealed that as the particle concentration increases from <500 to 1040000 mm^{-3}, the power transmittance ratio of the incident rays from a point source on a conjugate image region of the retina decreases from 1 to 0.0126, which corresponds to NO5. The concentration is close to that found in van den Berg's data: 525000 mm^{-3} for nuclear cataractous lens #96 with NO of 5.0 and NC of 6.2 [14]. The simulated large-particle concentrations for each NO grade are listed in the final column of Table I.

TABLE I
RELATIONSHIPS AMONG NUCLEAR CATARACT TYPE, VISUAL ACUITY, AND SIMULATED PARTICLE CONCENTRATION

NO Type	LogMAR	Snellen	Acuity	Log I	Lambert	Nits	Relative T. R.	Particle Con. (#/mm^3)
Healthy	-0.079	20/16.67	1.2	0.2	0.001585	5.045	1	<500
1	-0.07	20/17.02	1.18	0.02	0.001047	3.333	0.6607	75,000
2	0.08	20/24.05	0.83	-0.54	0.000288	0.918	0.1820	330,000
3	0.22	20/33.19	0.60	-0.99	0.000102	0.326	0.0646	580,000
4	0.38	20/47.98	0.42	-1.5	3.16E-05	0.101	0.0200	900,000
5	0.52	20/66.23	0.30	-1.7	2E-05	0.064	0.0126	1,040,000
6	0.67	20/93.55	0.21	-2	0.00001	0.032	0.0063	1,230,000

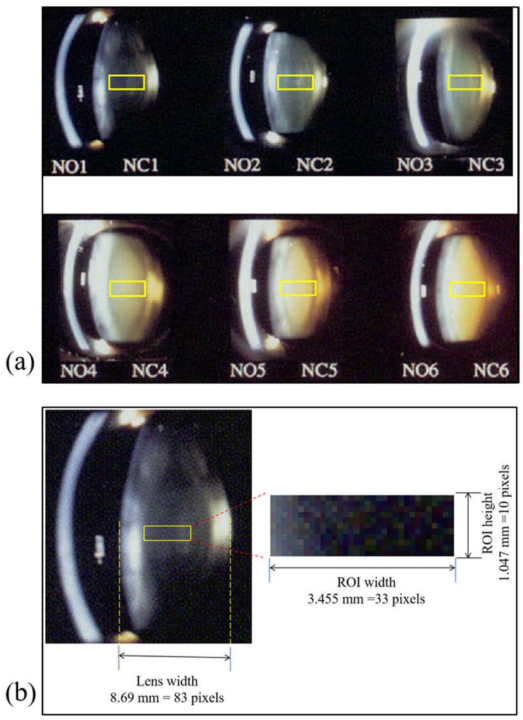

Fig. 2. (a) Slit-lamp photos showing nuclear cataracts of six LOCS III grades [7], with the ROI in each photo indicated by a yellow rectangle. (b) The dimensions of each yellow rectangle in the original picture are 33 pixels wide and 10 pixels high, which is equivalent to a field of view of approximately 3.455 mm in width and 1.047 mm in height.

B. Luminance and Color Analysis of Six Slit-Lamp Photos Correlated With Six Grades of Nuclear Cataract

LOCS III, the standard for visually evaluating the opacity of lenses with nuclear cataracts, guided the development of our model. The colorimetric properties of the nuclear cataracts, specifically, their chromaticity and luminance factor, are encapsulated by yellow squares in Fig. 2(a) and serve as the benchmark parameters for each region of interest (ROI). We implemented the following steps in our analysis:

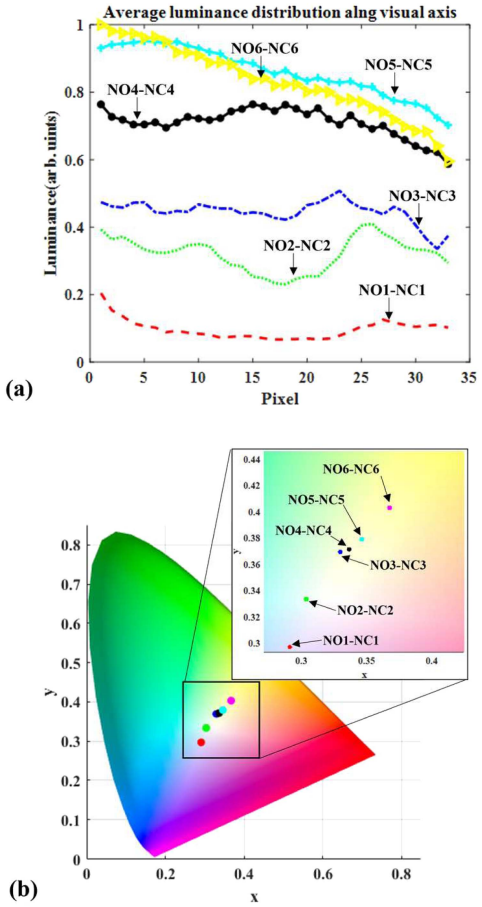

Fig. 3. (a) Average luminance distribution along the visual axis for different NO-NC grades and (b) corresponding centroid of CIE chromaticity coordinates.

1) defining the ROI, which is necessary because the extent of NO and NC changes significantly with LOCS III grade;
2) converting the RGB pixel values of each ROI to CIE 1931 XYZ tristimulus values;
3) averaging the tristimulus values in the vertical direction (i.e., leaving a row of tristimulus values along the visual axis); and
4) converting the average tristimulus values further into chromaticity pairs (x,y) by using (1) and retaining the luminance factor Y.

$$x = \frac{\mathrm{X}}{X+Y+Z}$$
$$y = \frac{\mathrm{Y}}{X+Y+Z}$$
$$\mathrm{z} = \frac{\mathrm{Z}}{X+Y+Z} = 1-x-y \tag{1}$$

As shown in Fig. 2(b), the ROI was situated between the anterior and posterior poles, with dimensions of approximately 3.455 mm (or 33 pixels) in width and 1.047 mm (or 11 pixels) in height. The average luminance distribution along the width direction for each grade is shown in Fig. 3(a). The average luminance for NO1-NC1 to NO6-NC6 is 0.07, 0.23, 0.32, 0.51, 0.62, and 0.60. From NO1-NC1 to NO4-NC4, the luminance is close to a constant along the visual axis because the concentration of scattering particles is low, meaning light is often scattered only once (single scattering). After NO5-NC5, the average luminance is higher, but the luminance along the visual axis of the ROI decreases gradually due to the high number of scattering particles. As a result, most rays are scattered several times within the initial length of the light's path through the ROI.

Fig. 3(b) presents the average chromaticity distribution for grades NO1-NC1 to NO6-NC6. As the grade increases, the corresponding chromaticity points in the CIE 1931 chromaticity diagram gradually shift from the white to the yellow region. The average relative luminance, CIE-x, and CIE-y for NO1-NC1 to NO6-NC6 in the ROI are listed in Table II. In summary, the curves in Fig. 3(a) and the chromaticity coordinates in Fig. 3(b) can be used to grade nuclear cataracts based on the luminance and chromaticity of the ROI.

TABLE II
AVERAGE RELATIVE LUMINANCE, CIE-x, AND CIE-y FOR NO1-NC1 TO NO6-NC6 IN THE ROI

Grade	Average relative luminance	Average Cx	Average Cy
NO1-NC1	0.1166	0.2911	0.2971
NO2-NC2	0.3858	0.3038	0.3336
NO3-NC3	0.5356	0.3297	0.3695
NO4-NC4	0.8539	0.3365	0.3716
NO5-NC5	1.0356	0.3462	0.3792
NO6-NC6	1.0000	0.3672	0.4032

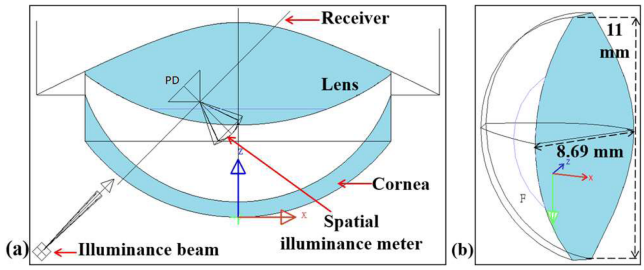

Fig. 4. Schematic layout showing the positioning of the illuminating beam and the spatial luminance meter. (a) Top view; (b) side view.

C. Modeling of Backward Scattering by Small Particles

To simulate backward scattering, an optical layout corresponding to slit-lamp observations was created and is illustrated in Fig. 4. A halogen slit beam open to 1 mm wide was simulated to project a thin sheet of light onto the posterior pole of the crystalline lens. A virtual spatial luminance meter simulated the role of the microscope, with the receiver acting as the object plane of the microscope's sensor. The receiver's field of view inside the lens measures 8.69 mm in width and 11 mm in height. Inside the model lens, small scattering particles with a radius of 10 nm were uniformly distributed. Using data from van den Berg [14], we determined that the highest small-particle concentration is 3.236×10^{13} mm^{-3} for a lens with nuclear cataracts of NO

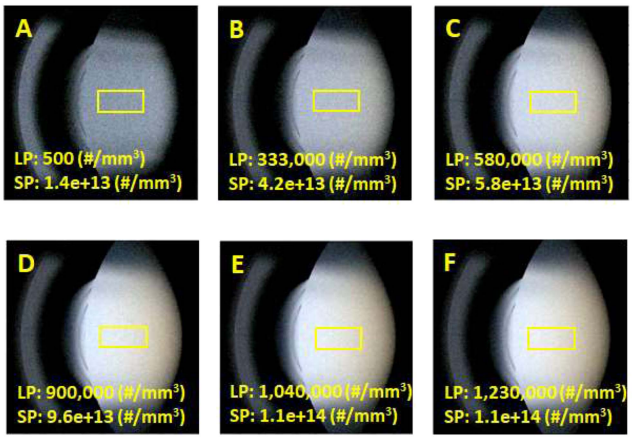

Fig. 5. Simulated photos of spatial luminance in the ROI in each photo delineated by a yellow rectangle. The respective concentrations of small and large scattering particles within the lens are listed at the bottom of each photo. Photos A to F display similar luminance distributions to those of the standard six slit-lamp photos for NO1-NC1 to NO6-NC6 [7]. LP = concentration of large particles. SP = concentration of small particles.

of 1.6 (NC 2.8) and 4.266 $\times$ 10^{14} mm^{-3} for NO of 5.0 (NC 6.2). The values imply that the small-particle concentration in a nuclear cataractous lens can reach 10^{14} mm^{-3}. To quantitatively assess the relation between small-particle concentration and each NO grade, we manipulated the small-particle concentration to generate a luminance distribution similar to that in Fig. 3(a). As the concentrations of small and large particles increase, more scattering in the plane of the receiver is directed away from the center of the lens, and the luminance is therefore greater (Fig. 5).

Fig. 6(a) shows the luminance distribution of the ROI in each simulated photo from Fig. 5. For cases A through D, the luminance distributions are similar to those of NO1-NC1 to NO4-NC4. Similarly, the luminance distribution in case F is similar to that for NO6-NC6. Our simulations suggest that the concentration of small scattering particles for grades NO1-NC1 to NO6-NC6 is between 1.4 $\times$ 10^{13} and 1.1 $\times$ 10^{14} mm^{-3}. However, the chromaticity coordinates of cases A through F (Fig. 6(b)) differ considerably from those of NO1-NC1 through NO6-NC6 (Fig. 3(b)) because the effect of the absorptive medium inside the large scattering particles is unaccounted for.

D. Modeling of Backward and Forward Scattering With Consideration Given to the Absorptive Medium

To match both the average luminance distribution along the visual axis and CIE chromaticity coordinates for various LOCS III NO-NC grades (Figs. 2 and 3), we further consider the effect of the absorptive medium inside the large scattering particles in the modeling by varying the wavelength-dependent behavior of absorption. Fig. 7 showcases the main results, presenting a comprehensive view of these dependencies through a combination of experimental measurements and simulation. Curve Ab-NC5 represents the absorption spectrum obtained from measurements published by Gaillard in 2000 [17]. The experimental measurement was conducted by measuring UV-visible spectra of a 78-year-old human lens sectioned at intervals along the

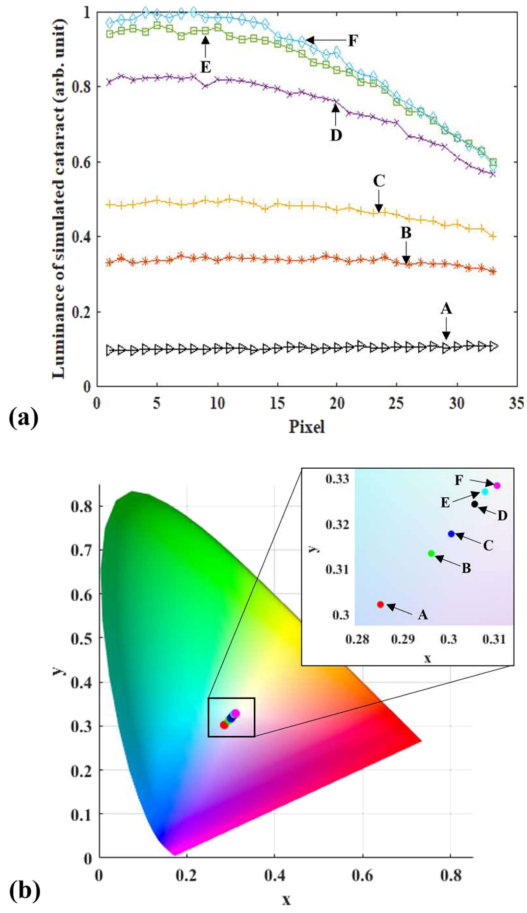

Fig. 6. (a) Average luminance distribution along the visual axis and (b) corresponding centroid CIE chromaticity coordinates for cases A to F.

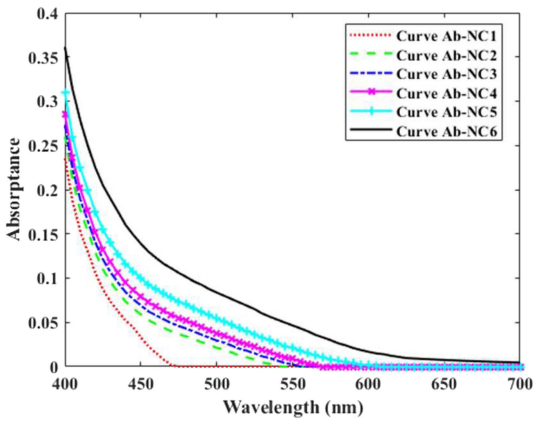

Fig. 7. Absorption spectrum curves Ab–NC1 to Ab–NC6 used for modeling NO1-NC1 to NO6-NC6.

visual axis and provide a baseline for understanding the large scattering particles' response to varying wavelengths of light. The spectrum of the whole lens exhibits a blue shift of its absorption maximum to approximately 400 nm, and the absorption of wavelengths as long as 700 nm monotonically decreases.

The remaining Curves (Ab-NC1, Ab-NC2, Ab-NC3, Ab-NC4 and Ab-NC6) were derived from Curve Ab-NC5 by varying

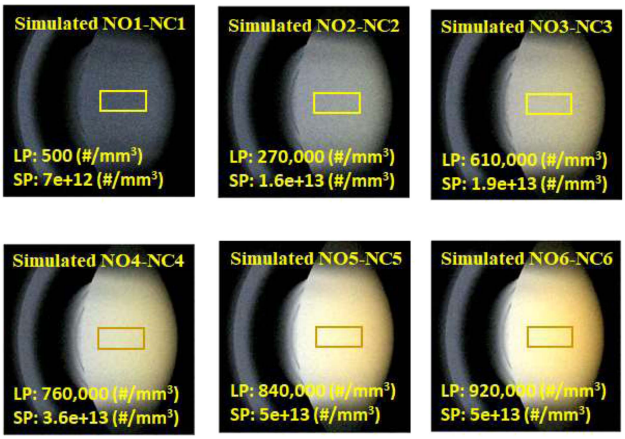

Fig. 8. Simulated images of six grades of nuclear cataracts.

the wavelength-dependent behavior of absorption to fit the corresponding luminance distribution and CIE chromaticity coordinates. Absorption increases from curve Ab-NC1 to curve Ab-NC6. An intriguing feature of the curves is the nearly monotonic wavelength dependence observed across all six. This behavior suggests a consistent trend in the pigment's response to different wavelengths, hinting a potential underlying mechanism governing its optical properties. The absorption spectrum $\alpha(\lambda)$, which ranges from 0 to 1, is a wavelength-dependent function indicating the probability that an incident ray passing through a large particle is absorbed. The wavelengths used to define the absorption spectrum must be a subset of the wavelengths traced in the LightTools model. In (2), the absorption is demonstrated to be wavelength dependent [18].

$$T_b\ (\lambda) = \exp\left(\frac{-D \cdot \alpha\,(\lambda)}{l}\right) \tag{2}$$

In this equation, D denotes the transmission path length, $\alpha(\lambda)$ the absorption spectrum, and l the mean free path, which is associated with the size and concentration of the large particles within the lens.

In the simulation, curves Ab–NC1 through Ab–NC6 were applied to model LOCS III grades NO1-NC1 to NO6-NC6. Fig. 8 illustrates the simulated nuclear cataract images for each grade, showing similarity with LOCS III images (Fig. 2). The average luminance distribution in Fig. 9(a) is close to that in Fig. 3(a), and the chromaticity coordinates in Figs. 3(b) and 9(b) deviate by less than 0.01 across all grades. The distribution of relative illuminance in Fig. 9(a) is smoother than that in Fig. 3(a) because both the smaller and larger scattering particles were assumed to be spherical and uniformly distributed in the simulation. This assumption enabled simplification and facilitated approximation; however, real cataractous particles are aspherical and have concentrations that vary locally inside the lens. The distribution of simulated NO6-NC6 in Fig. 9(a) exhibits a similar decline to that of NO6-NC6 in Fig. 3(a). In both distribution curves, the luminance value of pixel 33 is 34% lower than that of pixel 1. The values listed in Table III reveal several characteristics of the simulated nuclear cataract of each

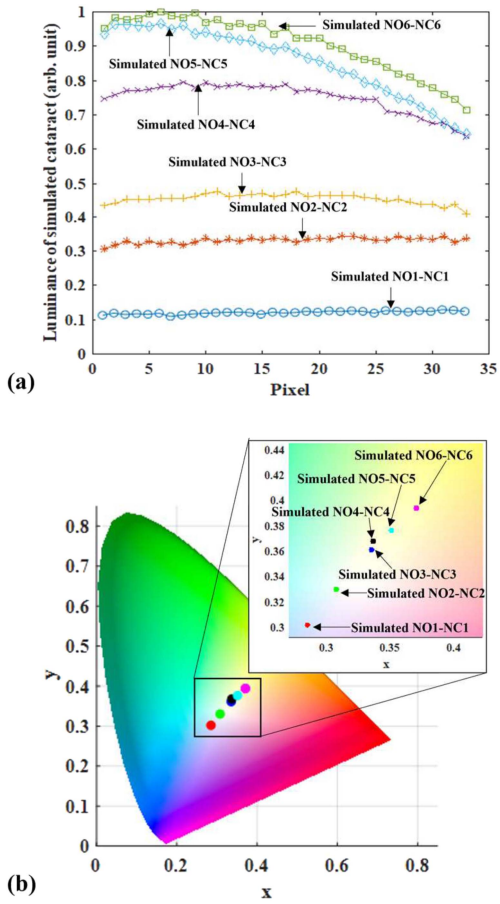

Fig. 9. (a) Average luminance distribution along the visual axis for simulated NO-NC grades and (b) corresponding centroid CIE chromaticity coordinates.

TABLE III
PARAMETERS USED FOR SIMULATING NO1-NC1 TO NO6-NC6 IN THE ROI

Types	Absorption spectra	Concentration of small scattering particles (#/mm³)	Concentration of large scattering particles (#/mm³)	Average x	Average y
Simulated NO1-NC1	Curve Ab-NC1	7.00E+12	500	0.28656	0.30797
Simulated NO2-NC2	Curve Ab-NC2	1.60E+13	270,000	0.30846	0.33286
Simulated NO3-NC3	Curve Ab-NC3	1.90E+13	610,000	0.33575	0.36303
Simulated NO4-NC4	Curve Ab-NC4	3.60E+13	760,000	0.33674	0.36832
Simulated NO5-NC5	Curve Ab-NC5	5.00E+13	840,000	0.34976	0.3761
Simulated NO6-NC6	Curve Ab-NC6	5.00E+13	920,000	0.37084	0.39417

grade. First, when the concentration of small scattering particles approaches 5.0×10^{13} mm^{-3}, the NO-NC grade reaches 5. Comparing with grade NO5-NC5, the concentration in NO6-NC6 keeps the same. Second, the maximum concentration of large scattering particles for grade 6 is 920000 mm^{-3}. Third, as the NO-NC grade increases, the concentrations of both the small and large scattering particles increase, but not linearly. Although the features of real nuclear cataracts are more complex, our simulations have potential for use in the modeling of scattering particles and absorption spectra. Based on the parameters listed in Table III, we further simulate images captured by the retina for grades NO1-NC1 to NO6-NC6. As shown in Fig. 10, an eye chart measuring 30.8 cm $\times$ 41 cm was positioned at an object distance of 40 cm and viewed by an eye model with optimal correction for

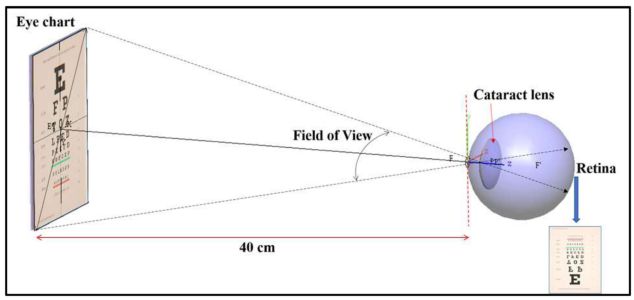

Fig. 10. Schematic of a human eye model with a cataract lens observing an eye chart placed 40 cm away, not to scale. The eye chart measures 30.8 cm × 41 cm, providing a field of view of 50 degrees to the eye.

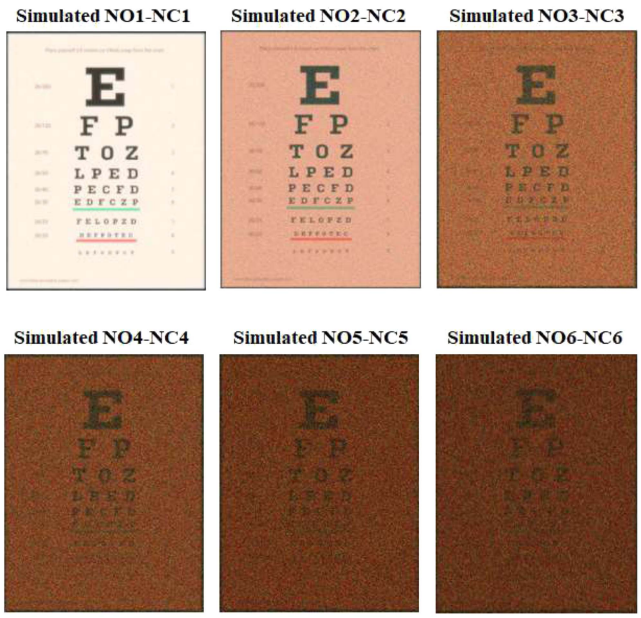

Fig. 11. Simulated images as captured by the retina for nuclear cataract grades NO1-NC1 to NO6-NC6.

nearsightedness. As the grade increase NO1-NC1 to NO6-NC6, the captured image on the retina becomes progressively more blurred and yellowish, which aligns with patient experiences (Fig. 11).

These simulations encompass a comprehensive consideration of both small and large scattering particles, as well as the absorption spectra. Consequently, our modeling facilitates the simultaneous simulation of interactions among these three critical factors. This multi-factorial simulation enhances the fidelity of our retina image simulations, bringing them closer to real-world conditions and enhancing the accuracy of our modeling. While our simulations provide valuable insights, it's important to acknowledge limitations. The original experimental data itself might have inherent uncertainties, and our simulation approach relies on assumptions and approximations that could introduce discrepancies.

Several approaches have been proposed to investigate the relationship between the conditions of nuclear cataracts and the visual function. A comparison of their features and outcomes is summarized in Table IV. Our method utilizes LOCS III images and incorporates previously measured data from References [14] and [17] in the modeling process, accounting for both small and large scattering particles, as well as the absorption spectra. In contrast, the method proposed in References [11] and [20] focuses solely on large scattering particles, excluding the effects of small scattering particles on the visual function. An observational study based on Scheimpflug images, as proposed in Reference [19], effectively correlates lens density with visual function. While both approaches—our LOCS III image-based method and the Scheimpflug image-based method—have demonstrated their effectiveness to some extent, a more comprehensive analysis that integrates the strengths of these two approaches may hold the potential to yield a more precise and realistic model.

TABLE IV
COMPARISON BETWEEN THE PROPOSED METHOD AND PRIOR ART

Reference	Approach	Feature	Outcome
Proposed method	LOCS III images–based Computational Model	Using optical software to establish the relationship between measured data (diameter, concentration, and color of cataract particles) and LOCS III images.	(a) Able to correlate the cataract particle condition with LOCS III; (b) Able to predict the retinal image of cataract patients.
[11]	Modeling light scattering of large cataract particles in the human eye	Investigating the effects of scattering particle diameter (ranging from 1 μm to 4 μm), particle concentration, and the wavelength of the illuminating light on the distribution of scattered light.	The size of the cataract particles is the most important parameter that affects the process of image formation on the retina.
[14]	Analysis of depth-dependent and wavelength-dependent light scattered from cataract lenses	By quantitatively determining the dependence on the wavelength and angle, as a function of depth, of light scattering in the human lens, the researchers can derive candidate particle distributions for nuclear light scattering.	The approach shows that the key particles causing forward light scattering are 692 nm average radius and occupy a tiny fraction of the volume.
[19]	Scheimpflug images based observational study	Studying average lens density (ALD) and nuclear lens density (NLD) using Scheimpflug imaging and exploring their potential correlations with visual function.	Able to correlate the conditions of ALD and NLD with LOCS III 、logarithmic minimal angle resolution (logMAR) for best-corrected visual acuity (BCVA), and contrast sensitivity (CS)
[20]	Forecasting light scattering in human age-related nuclear cataracts using Mie scattering theory	Applying Mie scattering theory to calculate scattering efficiencies for incident light with wavelengths (in vacuo) of 400, 550, and 700 nm.	Spherical particles that scatter light forward closely resembled the size of MLBs (multilamellar bodies) observed in cataractous nuclei by light miccroscopy and TEM.

III. CONCLUSION

A simple and robust optical model was constructed to simulate nuclear cataracts. The simulated results are quantitatively compatible with LOCS III after the elaboration of critical parameters (i.e., the concentrations and dimensions of small and large scattering particles and the absorptive characteristics of involved pigments). The maximum concentration of small scattering particles with a radius of 10 nm was 5.0×10^{13} mm^{-3}, and the maximum concentration of large scattering particles with a radius of 0.7 μm was approximately 920000 mm^{-3}. Moreover, the absorption of the pigments inside large particles increases with the grade of nuclear cataracts. Therefore, this method for modeling nuclear cataracts has the potential to help patients and clinicians quantitatively judge cataract severity.

ACKNOWLEDGMENT

The authors would like to thank Dr. George Chen of BC Photonics, Canada, for his valuable suggestions. We also thank Dr. Su Qiang of Tianjin Medical University for his manuscript review, Dr. Yu-Kuo Cheng of Chiao Tung University, Taiwan, for his expert assistance in color science and Prof. Han-Yin Sun of Chun Shang Medical University, Taiwan, for her advice on cataract evaluation methods. This manuscript was edited by Wallace Academic Editing.

REFERENCES

[1] P. A. Asbell, I. Dualan, J. Mindel, D. Brocks, M. Ahmad, and S. Epstein, "Age-related cataract," *Lancet*, vol. 365, pp. 599–609, Feb. 2005, doi: 10.1016/S0140-6736(05)17911-2.

[2] R. Truscott, "Age-related nuclear cataract-oxidation is the key," *Exp. Eye Res.*, vol. 80, pp. 709–725, May 2005, doi: 10.1016/j.exer.2004.12.007.

[3] T. J. van den Berg, "Intraocular light scatter, reflections, fluorescence and absorption: What we see in the slit lamp," *Ophthalmic Physiol. Opt.*, vol. 38, pp. 6–25, Jan. 2018, doi: 10.1111/opo.12426.

[4] K. O. Gilliland, C. D. Freel, C. W. Lane, W. C. Fowler, and M. J. Costello, "Multilamellar bodies as potential scattering particles in human age-related nuclear cataracts," *Mol. Vis.*, vol. 7, pp. 120–130, Jun. 2001.

[5] K. O. Gilliland, C. D. Freel, S. Johnsen, W. C. Fowler, and M. J. Costello, "Distribution, spherical structure and predicted mie scattering of multilamellar bodies in human age-related nuclear cataracts," *Exp. Eye. Res.*, vol. 79, pp. 563–576, Oct. 2004, doi: 10.1016/j.exer.2004.05.017.

[6] M. J. Costello, S. Johnsen, S. Metlapally, K. O. Gilliland, L. Frame, and D. Balasubramanian, "Multilamellar spherical particles as potential sources of excessive light scattering in human age-related nuclear cataracts," *Exp. Eye Res.*, vol. 91, pp. 881–889, Dec. 2010, doi: 10.1016/j.exer.2010.09.013.

[7] L. T. Chylack et al., "The lens opacities classification system III," *Arch. Ophthalmol.*, vol. 111, pp. 831–836, Jun. 1993, doi: 10.1001/archopht.1993.01090060119035.

[8] S. Lerman and O. Hockwin, "Automated biometry and densitomography of anterior segment of the eye," *Graefe's Arch. Clin. Exp. Ophthalmol.*, vol. 223, pp. 121–129, 1985, doi: 10.1007/BF02148887.

[9] M. B. Datiles III, B. V. Magno, and V. Freidlin, "Study of nuclear cataract progression using the national eye institute scheimpflug system," *Brit. J. Ophthalmol.*, vol. 79, pp. 527–534, Jun. 1995, doi: 10.1136/bjo.79.6.527.

[10] D. J. Spalton, R. A. Hitchings, P. A. Hunter, J. C. H. Tan, and J. Harry, *Atlas of Clinical Ophthalmology*, 3rd ed. Amsterdam, The Netherlands: Elsevier, 2004.

[11] I. Kelly-Pérez, N. C. Bruce, L. R. Berriel-Valdos, A. Werner, and J. A. Delgado Atencio, "Computational model of the effect of light scattering from cataracts in the human eye," *J. Opt. Soc. Amer. A Opt. Image Sci. Vis.*, vol. 30, pp. 2585–2594, Dec. 2013, doi: 10.1364/JOSAA.30.002585.

[12] LightTools, Synopsys. [Online]. Available: https://optics.synopsys.com/lighttools/

[13] B. H. Walker, *Optical Engineering Fundamentals*. New York, NY, USA: McGraw-Hill, 1995.

[14] T. van den Berg and H. Spekreijse, "Light scattering model for donor lenses as a function of depth," *Vis. Res.*, vol. 39, pp. 1437–1445, Jan. 1999, doi: 10.1016/S0042-6989(98)00220-X.

[15] E. Stifter, S. Sacu, A. Thaler, and H. Weghaupt, "Contrast acuity in cataracts of different morphology and association to self-reported visual function," *Invest. Ophthalmol. Vis. Sci.*, vol. 47, pp. 5412–5422, Dec. 2006, doi: 10.1167/iovs.05-1564.

[16] S. Hecht, "The relation between visual acuity and illumination," *J. Gen. Physiol.*, vol. 11, pp. 255–281, Jan. 1928, doi: 10.1085/jgp.11.3.255.

[17] E. R. Gaillard, L. Zheng, J. C. Merriam, and J. Dillon, "Age-related changes in the absorption characteristics of the primate lens," *Invest. Ophthalmol. Vis. Sci.*, vol. 41, pp. 1454–1459, May 2000.

[18] Z. Michael, "Phosphor modeling in LightTools," Synopsys white paper. Accessed: Oct. 11, 2023. [Online]. Available: https://www.synopsys.com/content/dam/synopsys/optical-solutions/documents/datasheets/modeling-phosphors-in-lighttools.pdf

[19] D. S. Grewal, G. S. Brar, and S. P. Grewal, "Correlation of nuclear cataract lens density using scheimpflug images with lens opacities classification system III and visual function," *Ophthalmology*, vol. 116, pp. 1436–1443, Aug. 2009, doi: 10.1016/j.ophtha.2009.03.002.

[20] M. J. Costello, S. Johnsen, K. O. Gilliland, C. D. Freel, and W. C. Fowler, "Predicted light scattering from particles observed in human age-related nuclear cataracts using Mie scattering theory," *Invest. Ophthalmol. Vis. Sci.*, vol. 48, pp. 303–312, Jan. 2007, doi: 10.1167/iovs.06-0480.